Role and Optimization of the Active Oxide Layer in TiO_2-Based RRAM

Anna Regoutz, Isha Gupta, Alexantrou Serb, Ali Khiat, Francesco Borgatti, Tien-Lin Lee, Christoph Schlueter, Piero Torelli, Benoit Gobaut, Mark Light, Daniela Carta, Stuart Pearce, Giancarlo Panaccione, and Themistoklis Prodromakis*

TiO_2 is commonly used as the active switching layer in resistive random access memory. The electrical characteristics of these devices are directly related to the fundamental conditions inside the TiO_2 layer and at the interfaces between it and the surrounding electrodes. However, it is complex to disentangle the effects of film "bulk" properties and interface phenomena. The present work uses hard X-ray photoemission spectroscopy (HAXPES) at different excitation energies to distinguish between these regimes. Changes are found to affect the entire thin film, but the most dramatic effects are confined to an interface. These changes are connected to oxygen ions moving and redistributing within the film. Based on the HAXPES results, post-deposition annealing of the TiO_2 thin film was investigated as an optimisation pathway in order to reach an ideal compromise between device resistivity and lifetime. The structural and chemical changes upon annealing are investigated using X-ray absorption spectroscopy and are further supported by a range of bulk and surface sensitive characterisation methods. In summary, it is shown that the management of oxygen content and interface quality is intrinsically important to device behavior and that careful annealing procedures are a powerful device optimisation technique.

1. Introduction

Materials science based on surface and interface effects has led to a tremendous theoretical and experimental effort, uncovering a wealth of new physics and anomalous properties at these spatial limits of the solid state. Presently, one of the most flourishing research fields and at the same time one of the major challenges faced by contemporary solid state science and technology has been in designing, understanding, and controlling the properties of engineered nanostructures and functional nanomaterials (e.g., oxides).[1] The choice of the materials, the optimization of the synthesis/growth/assembly, and the control/analysis of the critical physical parameters with chemical sensitivity remain open challenges for the realization of useful device structures.

In this context the memristor has come a long way since it was first postulated in 1971 by Chua.[2] From its theoretical definition as a "missing" fundamental passive circuit element,[3–5] through the development of the first devices capable of exhibiting "resistive switching" (the presently most popular engineering implementation of the "memristance" concept) by major industrial players,[6–8] to the study of the underlying physical characteristics underpinning resistive switching.[9–13] Developments in the field continue to be driven by the promise of resistive switches to eventually replace current memory technologies

Dr. A. Regoutz,[+] I. Gupta, Dr. A. Serb, Dr. A. Khiat, Dr. D. Carta, Dr. S. Pearce, Dr. T. Prodromakis
Nano Group, Southampton Nanofabrication Centre
Department of Electronics and Computer Science
University of Southampton
Southampton SO17 1BJ, UK
E-mail: a.regoutz@imperial.ac.uk

Dr. F. Borgatti
Consiglio Nazionale delle Ricerche – Istituto per lo Studio dei Materiali Nanostrutturati (CNR-ISMN)
via P. Gobetti 101, I-40129 Bologna, Italy

Dr. T.-L. Lee, Dr. C. Schlueter
Diamond Light Source Ltd.
Diamond House
Harwell Science and Innovation Campus
Didcot OX11 0DE, UK

DOI: 10.1002/adfm.201503522

Dr. P. Torelli, Dr. G. Panaccione
Consiglio Nazionale delle Ricerche – Istituto Officina dei Materiali (CNR-IOM)
Lab TASC, S.S.14, Km 163.5, I-34149 Trieste, Italy

Dr. B. Gobaut
Sincrotrone Trieste SCpA
Area Science Park, I-34149 Trieste, Italy

Dr. M. Light
Department of Chemistry
University of Southampton
Southampton SO17 1BJ, UK

[+]Present address: Department of Materials, Imperial College London, South Kensington, London SW7 2AZ, UK

such as NAND-flash by virtue of their extreme scalability[14] and potential for nonvolatile memory with long retention times,[15] high cycling endurance[16] and low operating power.[17]

TiO_2 based junction devices were one of the first semiconductor devices to be identified as memristors and have been studied extensively.[18–20] The study of such devices has now reached the state of device behavior optimization. A range of factors have been identified which directly influence the device performance and reliability, including annealing.[21] Although thermal annealing of TiO_2 thin films is very widely used in other applications, only very few reports have been published to date on the effect of post-deposition annealing of TiO_2 films for resistive random access memory (RRAM) applications. Kim and Rhee reported the effects of rapid thermal annealing (RTA) at temperatures of up to 800 °C, which lead to a change in the switching characteristics and breakdown mechanism.[22] RTA lead to mixed anatase/rutile polycrystalline films which showed high roughness and lost its memristive behavior at annealing temperatures of 600 °C and above. Contrary to this, Li et al. reported an improvement in resistive switching after RTA at 600 °C.[23]

This paper investigates the effects electrical switching of TiO_2-based RRAM has on the entire oxide layer as well as the interfaces between the oxide and the encompassing electrodes. By combining hard X-ray photoelectron spectroscopy (HAXPES) and X-ray absorption spectroscopy (XAS) measurements it is possible to investigate both the chemical and structural evolution of the TiO_2 thin film layer. Furthermore, thermal post-deposition annealing in a N_2/O_2 mixture is investigated as a method of optimization of the physical oxide characteristics to improve device behavior. It is found that the most dramatic changes are confined to distinct parts of the thin film stack and that a temperature induced transition from amorphous to crystalline TiO_2 has a significant influence on the electrical device behavior.

2. Results

TiO_2-based devices with a layout and stack as shown in **Figure 1**a were manufactured by standard device fabrication processes as outlined in the Experimental Section. HAXPES measurements of devices preset into distinct states, pristine (PRI), low-resistive (LRS), and high-resistive (HRS), were performed at the I09 beamline at the Diamond Light Source, UK. The X-ray beam

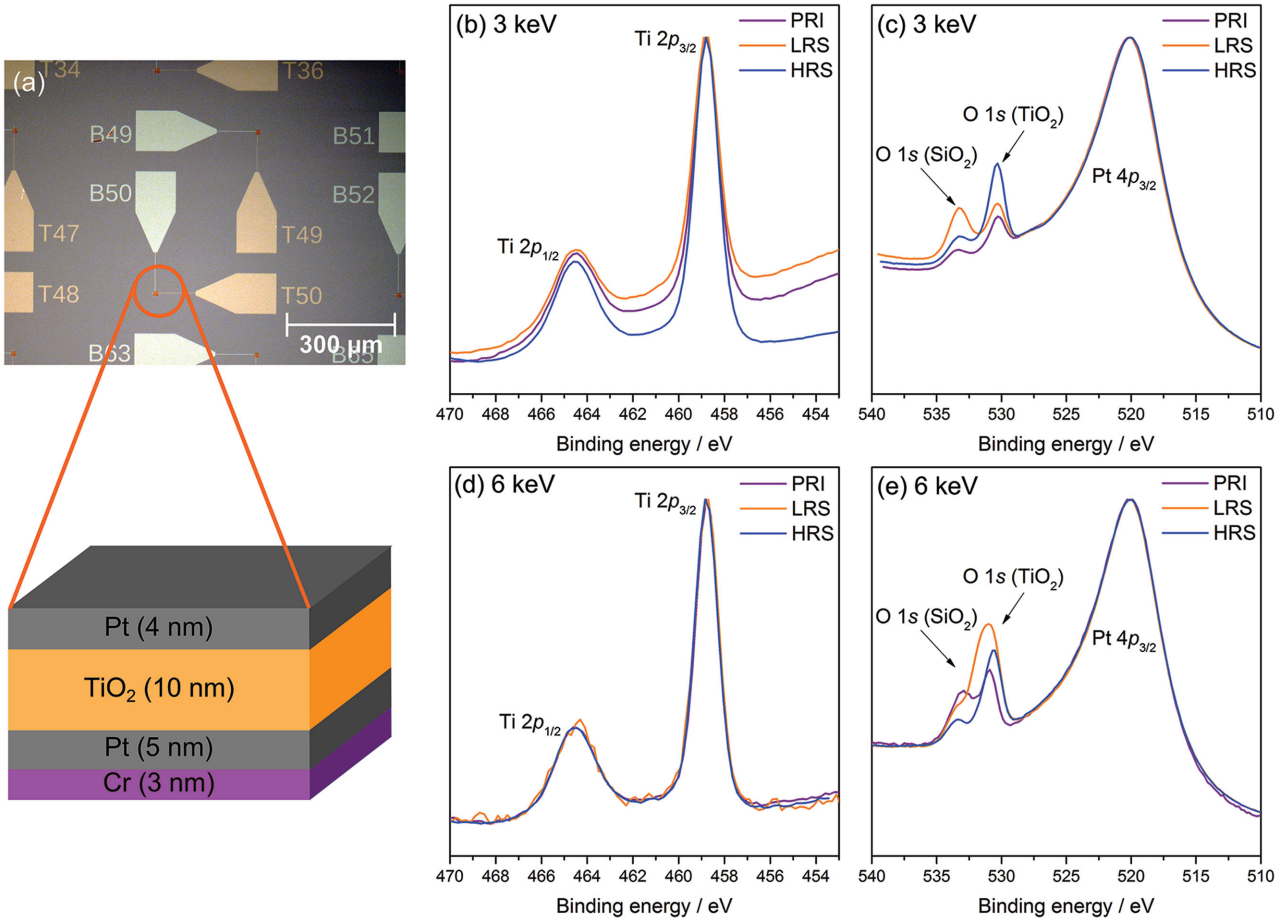

Figure 1. a) Optical image of the top view of a device pair. T and B refer to top and bottom electrodes, respectively. A single device is marked by the orange circle. The bottom schematic shows the thin film stack, with the active TiO_2 layer (10 nm thick) in between the electrodes (TE 4 nm and BE 5 nm thick). A 3 nm thin Cr seed layer is used beneath the BE. HAXPES spectra of b,d) Ti 2*p* and c,e) O1*s*/Pt $4p_{3/2}$ core levels in devices set to different distinct states (PRI: pristine state, LRS: low-resistive state, HRS: high-resistive state). Core levels collected both at 3 and 6 keV excitation energy are shown.

was aligned so that only a single device was probed at any one time. To address the question whether the entire TiO_2 film or only the interface to the electrodes changes, Ti 2*p* and O1*s* core level spectra were collected at two excitation energies, 3000 and 5935 eV (further referred to as 3 and 6 keV for simplicity). Whilst at 3 keV only the top half of the TiO_2 layer is probed, an excitation energy of 6 keV samples the entire bulk of the buried oxide layer (see device schematic in Figure 1a).[24]

The Ti 2*p* spectra at both energies (see Figure 1b,d)) show no significant changes (only a small change in the background is noted at 3 keV). No beam damage was observed over prolonged measurement periods, which is most likely due to the Pt electrode protecting the TiO_2 layer. Contrary to the behavior of the Ti 2*p* spectra, O 1*s* spectra change depending on the state of the device. These spectra were normalized to the intensity of the Pt $4p_{3/2}$ peak coming from the top electrode. Two O 1*s* components are visible; one belonging to the SiO_2 passivation of the Si wafer located around the active device area at a binding energy of 533 eV and a second peak at 530 eV consistent with oxygen in TiO_2. The SiO_2 peak was identified by comparative measurements on the Pt electrode running from connecting pads to the active device area, which only show the SiO_2, but not the TiO_2 contribution (see Figure S1, Supporting Information).

Focusing on the TiO_2 contribution to the O 1*s* signal, it becomes apparent that there is a different amount of oxygen ions present depending on the resistive state. Furthermore, this variation is not the same at 3 and 6 keV. The absence of significant changes to the Ti 2*p* core level suggests that the switching mechanism is predominantly mediated by oxygen ions.

In order to probe this point further, a fit analysis of the O 1*s*/Pt $4p_{3/2}$ region was carried out (see Table S1 of the Supporting Information for a summary of the fit parameters). This analysis allows the comparison of the different oxygen intensities occurring among the three resistive states. The oxygen intensity is normalized to the intensity of the Pt top electrode signal acting as a reference. **Figure 2** shows the fitted curves of the O 1*s*/Pt $4p_{3/2}$ core level spectra for both 3 and 6 keV. From these fits an order in terms of oxygen intensity I_O can be derived. For 3 keV it follows that $I_{O,PRI}(3) < I_{O,LRS}(4) < I_{O,HRS}(7)$ and for 6 keV $I_{O,PRI}(4) < I_{O,HRS}(7) < I_{O,LRS}(13)$.[25a,b,26] The HR state at both excitation energies shows a biasing induced increase of oxygen compared to the PRI state. Before biasing the oxygen is not evenly distributed over both probed sample volumes. The as-deposited TiO_2 thin films present in the PRI state are largely amorphous with a slightly nonuniform distribution of oxygen due to the nature of the reactive sputtering process, which is reflected in this variation of I_O. Contrarily, in HRS the same increased I_O is found

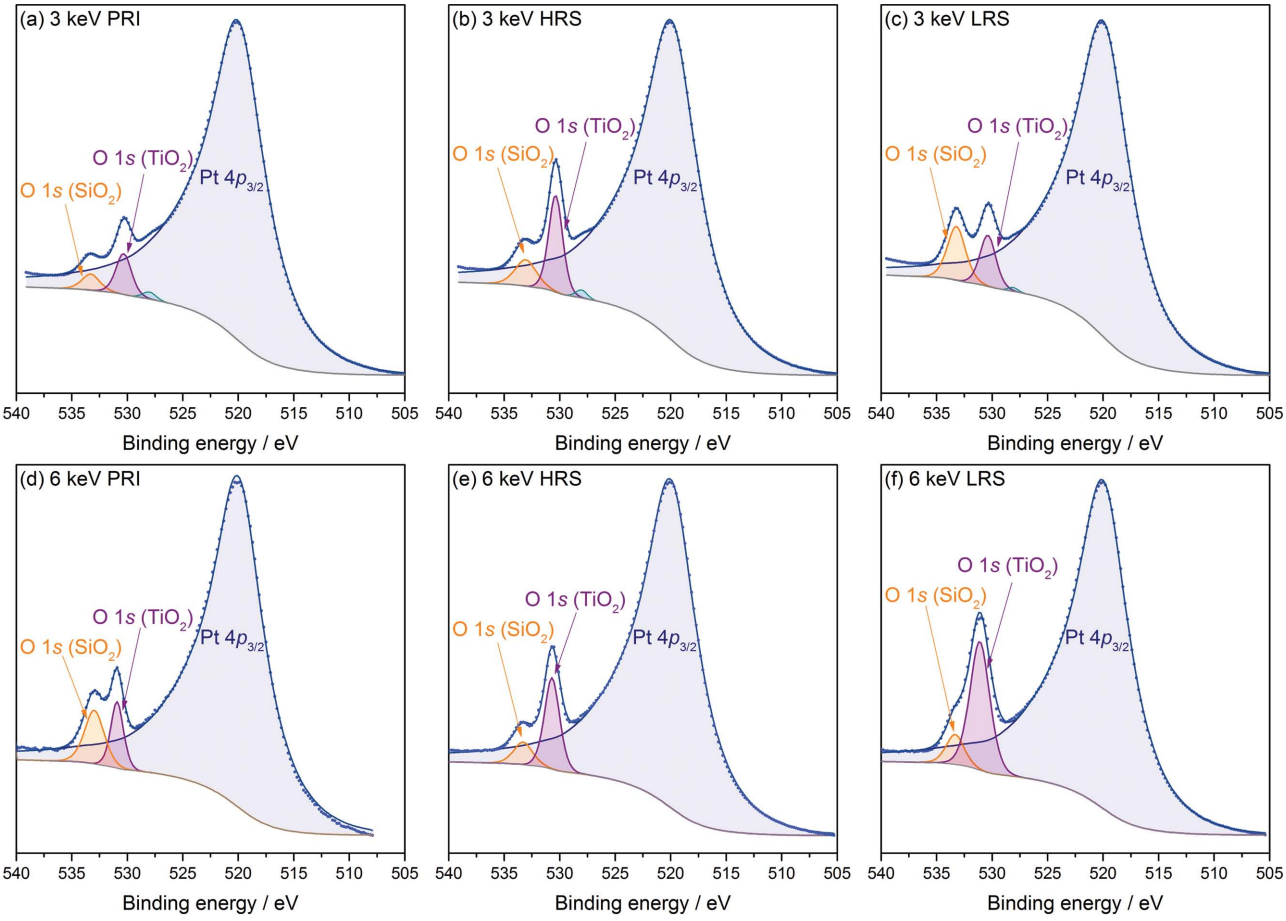

Figure 2. Fit analysis of HAXPES O 1*s*/Pt $4p_{3/2}$ core level spectra in devices set to different distinct states a,d) PRI: pristine state, b,e) LRS: low-resistive state, and c,f) HRS: high-resistive state. Core levels collected both at 3 and 6 keV excitation energy are shown.

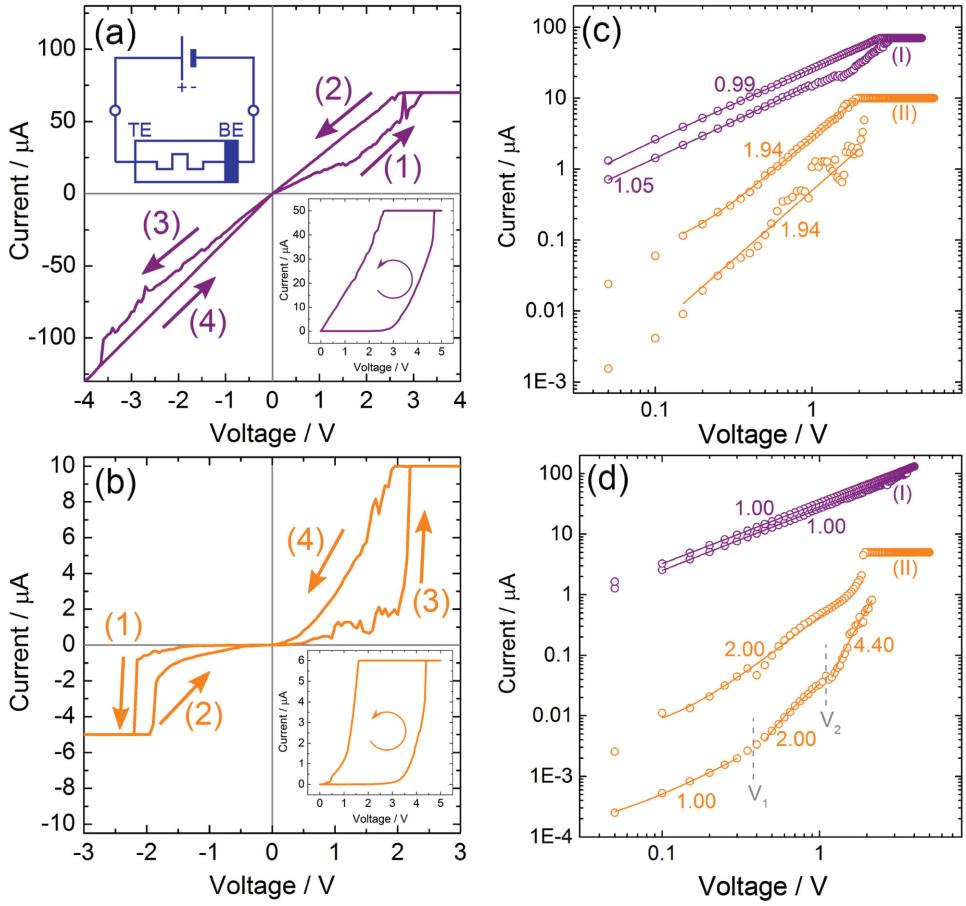

Figure 3. *I–V* characteristics of devices based on a) as-deposited and b) annealed thin films. The insets in the bottom right-hand corners show the electroforming curves. The top inset in (a) shows a schematic of the biasing circuit used. *I–V* curve fits c) for the positive bias voltage branches and d) corresponding negative branches for devices based on (I) as-deposited and (II) annealed thin films. The exponent of the current dependence of the voltage is given in the figures.

across the film volume. Biasing of a device leads to a redistribution of mobile oxygen species within the TiO_2. An increased amount of oxygen always goes hand in hand with an increase in resistivity resulting in HRS. Whilst this even distribution is found in HRS, a large disparity in I_O at different excitation energies was observed in LRS, where the bottom half of the oxide film is estimated to contribute ≈70% toward the overall I_O. Although some changes in I_O occur across the entire film thickness this extreme change suggests an interface rather than a bulk effect.

Based on the HAXPES results it becomes very clear that the management of oxygen content in the thin film is intrinsic to the device behavior. A method well established for other applications is post-deposition annealing of oxide layers to ensure stoichiometric and structural uniformity. In order to explore this method for RRAM, TiO_2-based devices were prepared both with as-deposited as well as annealed active oxide layers. The recorded *I–V*s are showing predominantly electronic current but are modulated by the much slower ionic transport. As-deposited devices exhibited typical forming voltages in the region of ±4–5 V (see insets in **Figure 3**a,b) with typical forming currents of 60–100 µA. However, annealed devices were 10 times more resistive than their as-deposited counterparts (see Figure 3), typically electroforming at ±2 V with much lower currents in the range of 10–20 µA (further electrical characteristics can be found in the Supporting Information). The lower electroforming voltages observed in devices based on annealed films could be related to the microstructural changes that occur during annealing, which can cause the formation of grain boundaries. Grain boundaries act as extended defects providing local conductive paths. The effects of grain boundaries on the behavior of RRAM devices has previously been reported for devices based on HfO_2 thin films.[27,28] Furthermore, the concave-up nonlinearity in the *I–V* characteristics below switching threshold is significantly more pronounced in annealed devices, whilst quasi-Ohmic *I–V*s are readily obtained in unannealed samples. This, in combination with the lower current draw at similar voltages renders annealed devices more suitable for use in crossbar arrays. The low current draw ensures low power operation whilst the ability of unannealed devices to draw disproportionately little current as bias voltage drops plays a role in mitigating the effects of sneak currents.[29,30]

The identification of the main charge transport modes for the devices has been carried out through fitting analysis of the *I–V* measurements. Figures 3c and Figure 3d show the logarithmic plot of the *I–V* data for the positive and negative voltage

regions, respectively, together with the fitting results obtained through the functional form $I \propto V^{\alpha}$. The values of the exponent are reported in the figures. Plotting the experimental results on logarithmic scales further evidences the differences among as-deposited and post-annealed devices. Ohmic conduction is dominating the entire voltage region for the as-deposited device, as is confirmed by the linear fitting dependence of the current on the voltage, except for a slight increase above 1.1 V in the positive voltage range before reaching the compliance current limit. The *I–V* characteristics of this device are therefore dominated by the contribution of the thermally generated free carriers inside the films, which is largely dominant over the injected carriers.[31] On the contrary, the post-annealed device shows a more complex behavior, particularly evident for the negative V polarities in which the *I–V* data are less noisy. The *I–V* characteristic (1) follows Ohm's law just for low applied voltage up to a threshold value of about $V_1 \approx 0.4$ V, then current raises up quadratically up $V_2 \approx 1.05$ V, and above V_2 a further increase of the slope to 4.4 is observed. Passing to branch (2) of the *I–V* cycle, the slope recovers the quadratic dependence, which is maintained also for positive applied voltages as shown in Figure 3c. The limited amount of experimental points does not allow to clearly state if the low voltage Ohmic behavior is present for all the *I–V* branches, however, it is reasonable to expect that it might occur for all of them. Focusing on the *I–V* quadratic dependence exhibited for most of the applied voltage range, the charge transport behavior of the post-annealed device can be identified as the space charge limited (SCL) conduction mechanism that, when it occurs without involving trapped states, can be described by the Child's law.[31] Therefore, the post-annealed device is passing from Ohmic to SCL conduction, i.e., above V_1 for branch (1), which implies that the injected excess carriers dominate over the thermally generated ones. The increase of the slope above V_1 suggests the passage to trap-assisted SCL conduction.[31] However, a larger amount of data is required to infer the distribution of the traps through proper modeling of the *I–V* characteristics.[32] The main result here is that the post-annealed device presents mostly SCL bulk dominated conduction, thus implying the relevance of post-deposition annealing in promoting structural and electronic changes of the TiO_2 layer.

The physical characteristics of the oxide layers in these devices were probed by XAS on thin film setups as described in the Experimental Section. The characteristics of the thin film setups were confirmed by XPS and XRR (see the Supporting Information for details). Ti $L_{2,3}$ and O K absorption spectra were collected both in total electron yield (TEY) and total fluorescence yield (TFY) at the APE beamline at Elettra Sincrotrone, Italy, (see **Figure 4**) hence being sensitive to either the upper region or the bulk of the sample similar to the HAXPES experiment. HAXPES measurements of the thin film samples showed a decrease of the population of Ti^{3+} atoms as well as surface hydroxide after annealing (see Figure S2 in the Supporting Information). The line shape of the spectra is strictly indicative of the chemical state of the Ti ions as well as the local ordering of the TiO_2 lattice. Both the L_3 and the L_2 edge are split in two distinct peaks, which is due to the t_{2g}–e_g ligand field splitting of the Ti 3*d* states. For the annealed film, the splitting of the e_g-related peak at about 455 eV, concerning the hybridization of the Ti ions with the surrounding oxygen atoms, is

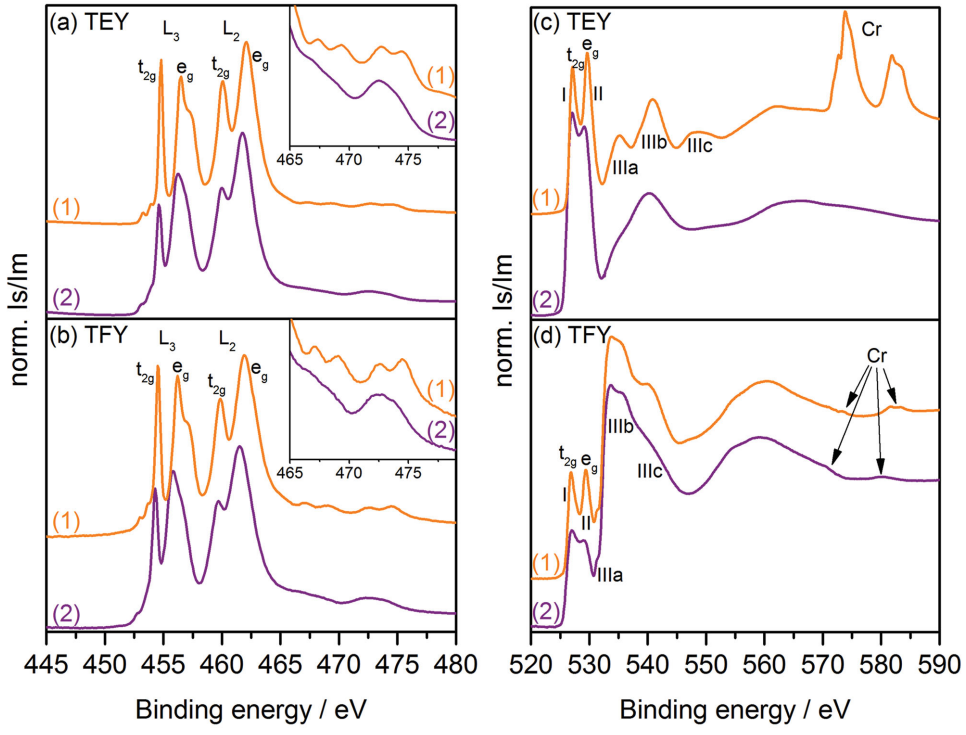

Figure 4. XAS data of annealed (1) and as-deposited (2) samples. a,b) The Ti L-edge and c,d) the O K-edge measured in both total electron yield (TEY) and total fluorescence yield (TFY). The insets in a,b) show a magnified view of the higher binding energy region.

strictly indicative of a high-quality anatase crystal phase (see Figure 4a,b). Conversely, its absence in the spectra of the as-deposited thin film indicates larger disorder, i.e., a more "amorphous" phase, implying the presence of many defects, e.g., oxygen vacancies (see Figure 4a). The annealing treatment promotes the improvement of the crystalline quality of the TiO_2 layer, with predominant formation of the anatase phase. This is in agreement with XRD results (see Figure S3a, Supporting Information).

The O K absorption edge, see Figure 4c,d closely reflects the distribution of unoccupied oxygen *p* states. The first two peaks at 527 and 529 eV correspond to transitions from O 1*s* to a mixed state of O 2*p* and Ti 3*d*. The occurrence of two peaks is due to the t_{2g}–e_g ligand field splitting of the Ti 3*d* states as noted above. The peak splitting as well as the intensity of the two peaks has been attributed to the degree of covalency.[33] For both TEY and TFY the pristine amorphous film shows a ligand field split Δ of 2.1 eV, whilst the annealed anatase films exhibits a higher value of 2.5 eV. These values agree perfectly with results from Räth et al. for 100 nm thick films prepared by ion beam induced CVD.[34] The peaks labeled IIIa–c between 532 and 555 eV in TEY mode are attributed to O *p* character states hybridized with metal states based on the same processes as the satellites on Ti peaks in both XPS and XAS. The observed peak shapes for the annealed sample and the broadening in the as-deposited sample agree with spectra reported for anatase and amorphous TiO_2 in the literature.[35–38] The difference in electrical behavior of devices based on as-deposited versus annealed TiO_2 thin films is due to the combination of changes in the oxygen content and in the structure of the films upon annealing.

The peaks between 570 and 590 eV in the TEY spectrum of the annealed sample are assigned to Cr 2*p* states. The different strength of these Cr $L_{2,3}$ absorption thresholds for the TEY and TFY spectra with respect to the oxygen demonstrate that the annealing promotes the segregation of chromium at the surface of the TiO_2. The peak characteristics fit well with references in the literature for Cr_2O_3.[39–41] This is confirmed by AFM measurements, which clearly show the Cr_2O_3 crystals on top of the TiO_2 thin film (see Figure S4, Supporting Information). These results in combination with the electrical characterization suggest that Cr segregates mostly at the surface of TiO_2 and does not affect the charge transport across this layer very significantly.

3. Conclusion

HAXPES measurements at different excitation energies enable the investigation of changes in TiO_2-based RRAM devices upon switching of the resistive state. Although some changes affect the entire thin film region, the most dramatic change for LRS is found in the bottom region of the device. It could be shown that oxygen ions were moving and redistributing within the film. Annealing of the initially amorphous TiO_2 film leads to the formation of highly uniform anatase thin films. Devices based on annealed films show a change in switching behavior compared to devices based on as-deposited oxide films, which can be correlated to a change in the oxygen content as well as a change from amorphous to anatase crystal phase as shown with XAS. The changes in device performance after annealing make them more suitable for low power operation and integration in crossbar arrays. *I–V* curves show no strong contribution of the interface, meaning that a space charge limited (SCL) conduction mechanism dominates the transport. The results presented here confirm the importance of thin film quality with regard to the oxygen content and provide evidence that a fine control of post-deposition annealing offers a strong way to tune the resistive switching behavior in oxide-based RRAM devices.

4. Experimental Section

Sample Preparation: High quality TiO_2 thin films with a thickness of 25 nm were prepared by lambda controlled plasma assisted reactive magnetron sputtering at room temperature. The substrate was prepared to mimic the layers present in a RRAM device. A (100)-oriented Si wafer with 200 nm thermal oxide was used as the substrate. For the bottom electrode (BE) a 3 nm Cr adhesion layer and a 5 nm Pt layer were deposited by electron beam evaporation. Two films, one as-deposited and one annealed in a mixture of 4 slm N_2 and 1 slm O_2, at 600 °C for 5 h with a heating and cooling rate of 5 °C min^{-1}, were prepared. Devices based on 10 nm TiO_2 films were produced in the same fashion as the thin films, but included the deposition of a 4 nm Pt top electrode (TE) and photolithography steps to pattern the device architecture appropriately.

Physical Characterization: HAXPES spectra were collected at the I09 beamline at the Diamond Light Source, UK. A liquid nitrogen cooled Si(111) double crystal monochromator was used to select 3 and 6 keV photons. To achieve a comparable energy resolution for both energies a Si(004) channel-cut crystal was employed as a post monochromator for the measurements at 6 keV. The resulting total experimental resolution was ≈300 meV for both photon energies. The end station is equipped with a VG Scienta EW4000 electron analyzer with ±30° angular acceptance. All experimental data are shown with energy scales referenced to the Fermi edge of Au references measured before and after scans. Particular attention was paid to align the focussed beam spot (15 × 30 μm^2) with the individual devices to ensure that only photoelectrons from one RRAM device were detected. At the chosen incidence angle the footprint of the beam could be aligned well within a single device (≈30 × 100 μm^2).

XPS–XAS experiments were performed on the APE-IOM surface laboratory and beamlines at the ELETTRA storage ring of Sincrotrone Trieste, in an ultrahigh vacuum (UHV) chamber with a base pressure of about 3×10^{-10} mbar.[42] Core level XPS spectra were measured by an Omicron EA-125 electron analyser on the HE-branch of the beam line, with an overall (photon and analyzer) energy resolution of 300 meV. All measurements have been performed at room temperature. Absorption spectra of the Ti $L_{2,3}$ and O K edges were recorded both in TEY, which probes roughly the first 5 nm of the sample surface, collecting the drain current from the sample and in TFY mode, which is more bulk sensitive, probing a depth of about 1 μm, revealing the fluorescence yield by means of a photodiode. Simultaneously, a mesh current proportional to the incoming photon flux was acquired in order to normalize the spectra.

Electrical Characterization: 1 × 1 μm^2 devices were electrically characterized by voltage sweeping using a Keithley 4200 probe station. Voltage sweeps of progressively higher peak voltage were applied under compliance current protection until the device under test electroformed. Bipolar switching was subsequently achieved by similar, progressively more invasive voltage sweeps of appropriate polarity.

Supporting Information

Supporting Information is available from the Wiley Online Library or from the author.

Acknowledgements

The authors thank Diamond Light Source for access to beamline I09 (SI10240) that contributed to the results presented here. This work was in part funded by the Italian Ministry of Research through the project PRIN "Interfacce di ossidi: nuove proprietà emergenti, multifunzionalità e dispositivi per l'elettronica e l'energia (OXIDE)." Financial support from the "Progetto Strategico di ricerca di interesse nazionale NFFA" MIUR n. B91J12000310001 is gratefully acknowledged. The authors acknowledge the financial support of EP/K017829/1 and EU-FP7 RAMP. Equipment grant (EP/K00509X/1) for the SmartLab.
The data for this paper can be found at 10.5258/SOTON/385174. The Acknowledgements have been updated on Jan 25th, 2016.

Received: August 20, 2015
Revised: October 22, 2015
Published online: December 15, 2015

[1] S. B. Ogale, T. V. Venkatesan, M. G. Blamire, *Functional Metal Oxides: New Science and Novel Applications*, Wiley-VCH, Weinheim, Germany **2013**.
[2] L. O. Chua, *IEEE Trans. Circuit Theory* **1971**, *18*, 507.
[3] L. O. Chua, S. M. Kang, *Proc. IEEE* **1976**, *64*, 209.
[4] D. B. Strukov, J. L. Borghetti, R. S. Williams, *small* **2009**, *5*, 1058.
[5] Y. N. Joglekar, S. J. Wolf, *Eur. J. Phys.* **2009**, *30*, 661.
[6] J. J. Yang, M. D. Pickett, X. Li, D. A. A. Ohlberg, D. R. Stewart, R. S. Williams, *Nat. Nanotechnol.* **2008**, *3*, 429.
[7] J. J. Yang, J. Borghetti, D. Murphy, D. R. Stewart, R. S. Williams, *Adv. Mater.* **2009**, *21*, 3754.
[8] M.-J. Lee, C. B. Lee, D. Lee, S. R. Lee, M. Chang, J. H. Hur, Y.-B. Kim, C.-J. Kim, D. H. Seo, S. Seo, U-I. Chung, I.-K. Yoo, K. Kim, *Nat. Mater.* **2011**, *10*, 625.
[9] F. Miao, J. P. Strachan, J. J. Yang, M.-X. Zhang, I. Goldfarb, A. C. Torrezan, P. Eschbach, R. D. Kelley, G. Medeiros-Ribeiro, R. S. Williams, *Adv. Mater.* **2011**, *23*, 5633.
[10] Y. Yang, P. Gao, S. Gaba, T. Chang, X. Pan, W. Lu, *Nat. Commun.* **2012**, *3*, 732.
[11] J. P. Strachan, J. J. Yang, L. A. Montoro, C. A. Ospina, A. J. Ramirez, A. L. D. Kilcoyne, G. Medeiros-Ribeiro, R. S. Williams, *Beilstein J. Nanotechnol.* **2013**, *4*, 467.
[12] A. Sawa, *Mater. Today* **2008**, *11*, 28.
[13] R. Waser, *J. Nanosci. Nanotechnol.* **2012**, *12*, 7628.
[14] B. Govoreanu, G. S. Kar, Y. Chen, V. Paraschiv, S. Kubicek, A. Fantini, O. P. Radu, L. Goux, S. Clima, R. Degraeve, N. Jossart, O. Richard, T. Vandeweyer, K. Seo, P. Hendrickx, G. Pourtois, H. Bender, L. Altimime, D. J. Wouters, J. A. Kittl, M. Jurczak, *IEEE Int. Electron Devices Meet* **2011**, *31*, 6.
[15] M.-J. Lee, C. B. Lee, D. Lee, S. R. Lee, M. Chang, J. H. Hur, Y.-B. Kim, C.-J. Kim, D. H. Seo, U.-I. Chung, I.-K. Yoo, K. Kim, *Nat. Mater.* **2011**, *10*, 625.
[16] J. J. Yang, M.-X. Zhang, J. P. Strachan, F. Miao, M. D. Pickett, R. D. Kelley, G. Medeiros-Ribeiro, R. S. Williams, *Appl. Phys. Lett.* **2010**, *97*, 232102.
[17] D. Ielmini, *IEEE Int. Electron Devices Meet.* **2011**, *17*, 2.
[18] H. Y. Jeong, J. Y. Lee, S.-Y. Choi, *Adv. Funct. Mater.* **2010**, *20*, 3912.
[19] K. M. Kim, G. H. Kim, S. J. Song, J. Y. Seok, M. H. Lee, J. H. Yoon, C. S. Hwang, *Nanotechnology* **2010**, *21*, 305203.
[20] K. Szot, M. Rogala, W. Speier, Z. Klusek, A. Besmehn, R. Waser, *Nanotechnology* **2011**, *22*, 254001.
[21] D. Acharyya, A. Hazra, P. Bhattacharyya, *Microelectron. Reliab.* **2014**, *54*, 541.
[22] W.-G. Kim, S.-W. Rhee, *Microelectron. Eng.* **2009**, *86*, 2153.
[23] Y. Li, Y. Wang, S. Liu, S. Long, H. Lv, Q. Liu, Q. Wang, S. Zhang, M. Liu, *J. Korean Phys. Soc.* **2011**, *58*, L407.
[24] M. Sacchi, F. Offi, P. Torelli, A. Fondacaro, C. Spezzani, M. Cautero, G. Cautero, S. Huotari, M. Grioni, R. Delaunay, M. Fabrizioli, G. Vankó, G. Monaco, G. Paolicelli, G. Stefani, G. Panaccione, *Phys. Rev. B* **2005**, *71*, 155117.
[25] a) S. Tanuma, C. J. Powell, D. R. Penn, *Surf. Interface Anal.* **1993**, *21*, 165; b) Both IMFP and cross sections contribute to the peak areas used to determine the oxygen intensity I_O. However, they do not alter the qualitative trends observed.
[26] J. H. Scofield, *Theoretical Photoionization Cross Sections from 1 to 1500 keV*, Lawrence Livermore National Laboratory, Report Number UCRL-51326, **1973**.
[27] I.-S. Mok, J. Kim, K. Lee, Y. Kim, H. Sohn, *J. Korean Phys. Soc.* **2014**, *64*, 419.
[28] M. Lanza, G. Bersuker, M. Porti, E. Miranda, M. Nafría, X. Aymerich, *Appl. Phys. Lett.* **2012**, *101*, 193502.
[29] J. Zhou, K.-H. Kim, E. Lu, *IEEE Trans. Electron Devices* **2014**, *61*, 1369.
[30] E. Linn, R. Rosezin, C. Kügeler, R. Waser, *Nat. Mater.* **2010**, *9*, 403.
[31] F.-C. Chiu, *Adv. Mater. Sci. Eng.* **2014**, *2014*, 578168.
[32] K. M. Kim, B. J. Choi, M. H. Lee, G. H. Kim, S. J. Song, J. Y. Seok, J. H. Yoon, S. Han, C. S. Hwang, *Nanotechnology* **2011**, *22*, 254010.
[33] E. Stoyanov, F. Langenhorst, G. Steinle-Neumann, *Am. Mineral.* **2007**, *92*, 577.
[34] S. Räth, F. Gracia, F. Yubero, J. P. Holgado, A. I. Martin, D. Batchelor, A. R. Gonzalez-Elipe, *Nucl. Instrum. Methods, B* **2003**, *200*, 248.
[35] G. Van der Laan, *Phys. Rev B* **1990**, *41*, 12366.
[36] S. O. Kucheyev, T. van Buuren, T. F. Baumann, J. H. Sacher, T. M. Willey, R. W. Meulenberg, T. E. Felter, J. F. Poco, S. A. Gammon, L. J. Terminello, *Phys. Rev. B* **2004**, *69*, 245102.
[37] I. Karatchevtseva, D. J. Cassidy, Z. Zhang, G. Triani, K. S. Finnie, S. L. Cram, C. J. Barbe, *J. Am. Chem. Soc.* **2008**, *91*, 2015.
[38] R. Gago, A. Redondo-Cubero, M. Vinnichenko, L. Vazquez, *Chem. Phys. Lett.* **2011**, *511*, 367.
[39] M. O. Figueiredo, A. C. dos Santos, M. J. Carmezim, M. Abbate, F. M. F. de Groot, H. Petersen, W. Braun, *Analyst* **1994**, *119*, 609.
[40] Y. S. Dedkov, A. S. Vinogradov, M. Fonin, C. König, D. V. Vyalikh, A. B. Preobrajenski, S. A. Krasnikov, E. Y. Kleimenov, M. A. Nesterov, U. Rüdiger, S. L. Molodtsov, G. Gliüntherodt, *Phys. Rev. B* **2005**, *72*, 060401(R).
[41] S. O. Kucheyev, B. Sadigh, T. F. Baumann, Y. M. Wang, T. E. Felter, T. van Buuren, A. E. Gash, J. H. Sacher, A. V. Hamza, *J. Appl. Phys.* **2007**, *101*, 124315.
[42] G. Panaccione, I. Vobornik, J. Fujii, D. Krizmancic, E. Annese, L. Giovanelli, F. Maccherozzi, F. Salvador, A. De Luisa, D. Benedetti, A. Gruden, P. Bertoch, F. Polack, D. Cocco, G. Sostero, B. Diviacco, M. Hochstrasser, U. Maier, D. Pescia, C. H. Back, T. Greber, J. Osterwalder, M. Galaktionov, M. Sancrotti, G. Rossi, *Rev. Sci. Instrum.* **2009**, *80*, 043105.